

Article

Facile Synthesis of a $\text{Bi}_2\text{WO}_6/\text{BiO}_{2-x}$ Heterojunction for Efficient Photocatalytic Degradation of Ciprofloxacin under Visible Light Irradiation

Hongzhong Zhang ^{1,*}, Zhaoya Fan ¹, Qingqing Chai ² and Jun Li ^{2,*} 

¹ School of Materials and Chemical Engineering, Zhengzhou University of Light Industry, Zhengzhou 450001, China

² Henan Institute of Advanced Technology, Zhengzhou University, Zhengzhou 450052, China

* Correspondence: zhz@zzuli.edu.cn (H.Z.); junli2019@zzu.edu.cn (J.L.)

Abstract: In this work, a Z-scheme $\text{Bi}_2\text{WO}_6/\text{BiO}_{2-x}$ heterojunction was successfully prepared using a self-assembly strategy. Various characterization techniques demonstrated that the formation of the heterojunction not only accelerated the separation of photoinduced carriers but also weakened the recombination rate of photogenerated electron–hole pairs. The $\text{Bi}_2\text{WO}_6/\text{BiO}_{2-x}$ composites had a wider absorption edge than Bi_2WO_6 in the range of 200–800 nm, which improved the photocatalytic performance of ciprofloxacin (CIP) degradation under xenon lamps. As a result, the Z-scheme heterojunction $\text{Bi}_2\text{WO}_6/\text{BiO}_{2-x}$ composite exhibited excellent photocatalytic activity. Catalyzed by the optimal 20% $\text{Bi}_2\text{WO}_6/\text{BiO}_{2-x}$ (0.5 g/L), the removal rate of CIP (10.0 mg/L) was 91.8% within 2 h irradiated by visible light, which was 2.37 times that of the BiO_{2-x} catalyst. This work will provide a fresh perspective on the construction of visible-driven Z-scheme photocatalysts for wastewater treatment.

Keywords: photocatalysis; ciprofloxacin; Bi_2WO_6 ; BiO_{2-x} ; Z-scheme heterostructure



Citation: Zhang, H.; Fan, Z.; Chai, Q.; Li, J. Facile Synthesis of a $\text{Bi}_2\text{WO}_6/\text{BiO}_{2-x}$ Heterojunction for Efficient Photocatalytic Degradation of Ciprofloxacin under Visible Light Irradiation. *Catalysts* **2023**, *13*, 469. <https://doi.org/10.3390/catal13030469>

Academic Editor: Zhenfeng Bian

Received: 19 January 2023

Revised: 10 February 2023

Accepted: 21 February 2023

Published: 23 February 2023



Copyright: © 2023 by the authors. Licensee MDPI, Basel, Switzerland. This article is an open access article distributed under the terms and conditions of the Creative Commons Attribution (CC BY) license (<https://creativecommons.org/licenses/by/4.0/>).

1. Introduction

Nowadays, antibiotics play an influential role in healthcare, agriculture and animal husbandry [1]. For example, ciprofloxacin (CIP), a second-generation quinolone antibacterial drug with broad-spectrum antibacterial and bactericidal activity, is commonly used to treat bacterial infections in humans and animals [2]. However, these drugs are not easily broken down in the living body; they remain in feces and eventually accumulate in rivers, pools and groundwater [3]. Through wastewater discharges and agricultural runoff, residual drugs can easily enter the aquatic environment, leading to the proliferation of drug-resistant bacteria that can lead to serious ecological risks [4]. It is imperative that antibiotics such as CIP should be removed from the ecosystem to ensure public and environmental health.

In recent years, photocatalysis has been regarded as an environmental purification technology that can effectively alleviate environmental problems due to its eco-friendly, safe and efficient characteristics [5,6]. Among the available photocatalyst materials, Bi_2WO_6 has attracted widespread attention owing to the low toxicity, favorable stability, and abundant oxygen defects [7]. Nonetheless, Bi_2WO_6 exhibits a high recombination rate of combined electron–hole pairs, which limits practical applications in environmental purification [8,9]. A series of strategies were attempted to alleviate the recombination rate of photogenerated electrons (e^-) and holes (h^+), including morphology control [10,11], doping [12], fabricating defective materials [13,14], and constructing heterojunctions [15,16]. It is prevalent to couple Bi_2WO_6 with the different functional materials to form heterostructures, which has been identified as the most useful approach. Among them, the construction of Z-scheme heterojunction has been proved to be an effective method to inhibit the recombination of

electron–hole pairs [17]. Successful cases include $\text{Bi}_2\text{WO}_6/\text{BiPO}_4$ [18], $\text{Bi}_2\text{WO}_6/\text{CdS}$ [19], $\text{Bi}_2\text{WO}_6/\text{CuBi}_2\text{O}_4$ [20], $\text{Bi}_2\text{WO}_6/\text{Ta}_3\text{N}_5$ [21], $\text{Bi}_2\text{WO}_6/\text{WO}_3$ [22], $\text{Bi}_2\text{WO}_6/\text{TiO}_2$ [23] and $\text{Bi}_2\text{WO}_6/\text{ZnO}$ [24], and so forth.

A surprising finding in recent years is that all inorganic bismuth-based compounds have bright prospects for solar energy conversion and environmental remediation [25–27]. Among these, BiO_{2-x} was extensively reported to be a promising candidate for photocatalytic applications due to its relatively narrow band gap and plentiful oxygen vacancies [28]. Meanwhile, owing to the existence of mixed Bi^{3+} and Bi^{5+} , BiO_{2-x} overcomes the drawbacks of inadequate light absorption range of a monovalent compound [29]. Bi_2WO_6 and BiO_{2-x} have received a lot of attention in the field of photocatalysis and wastewater treatment field due to their great potential for applications. However, few studies focus on the $\text{Bi}_2\text{WO}_6/\text{BiO}_{2-x}$ -based heterojunction photocatalysis for CIP degradation. At the same time, the mechanism of the photocatalytic reactions in binary bismuth systems with oxygen defects is still unclear.

Here, a series of Z-scheme $\text{Bi}_2\text{WO}_6/\text{BiO}_{2-x}$ heterostructures were fabricated using a facile electrostatic self-assembly process [30]. The photocatalytic performance of the catalysts was verified by measuring its photodegradation performance of CIP. The application of a number of catalysts to the photocatalytic degradation of ciprofloxacin is shown in Table S3, demonstrating that synthesized heterostructures have a prominent effect on the photocatalytic degradation of ciprofloxacin. Electrochemical tests and photoluminescence (PL) spectra proved that the participation of Bi_2WO_6 could effectively inhibit the recombination of photogenerated carriers in the $\text{Bi}_2\text{WO}_6/\text{BiO}_{2-x}$ heterojunction. In short, constructing $\text{Bi}_2\text{WO}_6/\text{BiO}_{2-x}$ heterojunction restrains the recombination of photogenerated carriers, therefore optimizing broad-spectrum driven photocatalytic activity [31]. In addition, based on the photocatalyst characterization and experimental evidence, this work provides a comprehensive understanding of the constructed Z-scheme heterojunction for CIP degradation processes and paves a possible way for the development of extremely efficient photocatalysts for wastewater treatment.

2. Results and Discussions

2.1. Synthesis and Characterization of Catalysts

The crystalline structures of the parent BiO_{2-x} , Bi_2WO_6 and $\text{Bi}_2\text{WO}_6/\text{BiO}_{2-x}$ composites were analyzed through their XRD patterns. As shown in Figure 1a, the characteristic peaks of BiO_{2-x} were located at $2\theta = 28.21^\circ$, 32.69° , 46.92° , 55.64° , and 58.54° , corresponding to the (111), (200), (220), (311), and (222) crystal faces, respectively (JCPDS NO. 47-1057) [32], whereas the peaks at $2\theta = 28.30^\circ$, 32.67° , 46.97° , 55.66° , and 58.33° were assigned to the (131), (060), (260), (191), and (262) planes of the Bi_2WO_6 crystal structure (JCPDS No. 39-0256) [33]. As shown in Table S1, we calculated the XRD data using the Scherrer formula, and found that the average grain size of the sample decreased with the increase in Bi_2WO_6 loading. The decrease of catalyst grain size will increase the specific surface area, which can further increase the contact area with the reactant and thus improve the photocatalytic performance. The increase in FWHM in $\text{Bi}_2\text{WO}_6/\text{BiO}_{2-x}$ is attributed to lattice strain in the heterostructure, which may be due to the doping [17]. The $\text{Bi}_2\text{WO}_6/\text{BiO}_{2-x}$ composites displayed similar structural features to BiO_{2-x} and Bi_2WO_6 . It reveals that the crystal structure of the composite remains stable during synthesis, further confirming the heterostructure formation of $\text{Bi}_2\text{WO}_6/\text{BiO}_{2-x}$.

The FT-IR spectra of a series of $\text{Bi}_2\text{WO}_6/\text{BiO}_{2-x}$ composites exhibited similar vibration modes to BiO_{2-x} , suggesting small amounts of Bi_2WO_6 combined with BiO_{2-x} did not affect the chemical structure of BiO_{2-x} (Figure 1b). In the spectrum of BiO_{2-x} , the absorption peaks at 519 cm^{-1} , 589 cm^{-1} and 954 cm^{-1} belonged to the stretching vibrations of the Bi-O bond [33]. For Bi_2WO_6 , the characteristic peaks at 589 cm^{-1} and 687 cm^{-1} could be ascribed to the stretching vibration of Bi-O and W-O [34]. The peak at 1389 cm^{-1} was associated with the W-O-W bridging stretching of Bi_2WO_6 [35]. There were two signal peaks located at 1635 cm^{-1} and 3421 cm^{-1} that belong to the stretching and bending vibrations of the

O-H functional groups resulting from the adsorption water, respectively [36]. All these characteristic peaks of BiO_{2-x} and Bi_2WO_6 existed in their composites, which proved that $\text{Bi}_2\text{WO}_6/\text{BiO}_{2-x}$ heterojunction had been successfully formed.

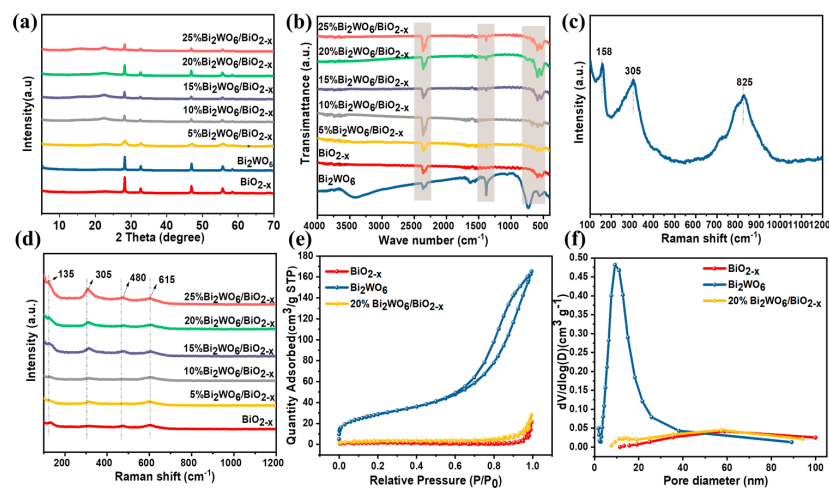


Figure 1. (a) XRD patterns and (b) FT-IR spectra of BiO_{2-x} , Bi_2WO_6 and $\text{Bi}_2\text{WO}_6/\text{BiO}_{2-x}$ composites. Raman spectra of (c) Bi_2WO_6 , (d) BiO_{2-x} and $\text{Bi}_2\text{WO}_6/\text{BiO}_{2-x}$ composites. (e) N_2 adsorption–desorption isotherms and (f) BJH pore diameter distribution of BiO_{2-x} , Bi_2WO_6 and 20% $\text{Bi}_2\text{WO}_6/\text{BiO}_{2-x}$.

Furthermore, Figure 1c shows the Raman spectroscopy of Bi_2WO_6 . For the pure Bi_2WO_6 sample, the peaks at 158 cm^{-1} , 305 cm^{-1} and 825 cm^{-1} were assigned to the Bi-O, the bending vibrations mode of BiO_6 polyhedron and the symmetric stretching vibration of O-W-O [37,38]. Figure 1d shows the Raman spectra of BiO_{2-x} and a series of $\text{Bi}_2\text{WO}_6/\text{BiO}_{2-x}$ composites ranging from 100 cm^{-1} – 1200 cm^{-1} . The peaks at approximately 135 cm^{-1} , 480 cm^{-1} and 615 cm^{-1} could be ascribed to the Bi-O stretches of BiO_{2-x} [39]. With the increase in content of Bi_2WO_6 in the composites, the intensity of the peak at 305 cm^{-1} also increased, indicating that the $\text{Bi}_2\text{WO}_6/\text{BiO}_{2-x}$ heterojunction was successfully synthesized.

To acquire the porous characteristics of the obtained materials, we proceeded with N_2 adsorption–desorption experiments for BiO_{2-x} , Bi_2WO_6 and 20% $\text{Bi}_2\text{WO}_6/\text{BiO}_{2-x}$. Figure 1e and Table S2 displayed the N_2 adsorption–desorption isotherms of the samples; the specific surface area of BiO_{2-x} , Bi_2WO_6 and 20% $\text{Bi}_2\text{WO}_6/\text{BiO}_{2-x}$ were $5.1639\text{ m}^2\text{ g}^{-1}$, $101.5031\text{ m}^2\text{ g}^{-1}$ and $10.4902\text{ m}^2\text{ g}^{-1}$. According to the IUPAC classification, all of the materials exhibited type IV isotherms featured with type H3 hysteresis loops, suggesting these samples contain abundant mesoporous [40,41]. The porous features can be further found in their pore size distribution curves shown in Figure 1f; the pore sizes of Bi_2WO_6 , BiO_{2-x} and 20% $\text{Bi}_2\text{WO}_6/\text{BiO}_{2-x}$ were dispersed between 8.7 and 53.7 nm. Obviously, the specific surface area of 20% $\text{Bi}_2\text{WO}_6/\text{BiO}_{2-x}$ was approximately twice that of pure BiO_{2-x} , indicating that the composites had more active sites and were beneficial to enhancing photocatalytic performance.

Figure S1a shows the typical nanosheet morphology of the BiO_{2-x} nanostructure. Bi_2WO_6 is formed by the accumulation of a large number of nanosheets (Figure S1b). Figure S1c and Figure 2a show the SEM and TEM images of 20% $\text{Bi}_2\text{WO}_6/\text{BiO}_{2-x}$, which prove that Bi_2WO_6 nanosheets are loaded on BiO_{2-x} nanosheets successfully. The HRTEM images (Figures 2b and S2b) show the lattice stripes of 0.315 nm, corresponding to the (111) crystal plane of BiO_{2-x} nanosheets. Moreover, Figures 2b and S2d show that the calculated d space values 0.375 nm and 0.226 nm are attributed to the (111) plane and (042) plane of Bi_2WO_6 . EDS elemental analysis (Figure S3), and the elemental mapping images (Figure 2d–f) of 20% $\text{Bi}_2\text{WO}_6/\text{BiO}_{2-x}$ reveal homogeneous distribution of Bi, O, and W

elements in the sample, which is highly in accordance with the results of TEM images and indicates the formation of $\text{Bi}_2\text{WO}_6/\text{BiO}_{2-x}$ heterojunction.

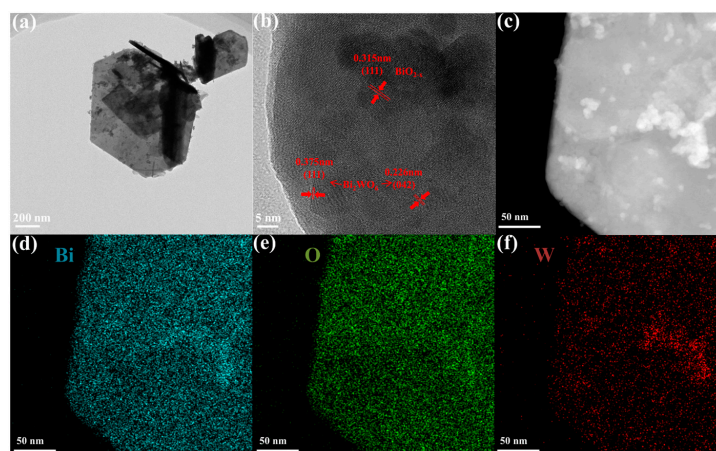


Figure 2. (a) TEM image; (b) HRTEM image; (c) HAADF image and elemental mapping of 20% $\text{Bi}_2\text{WO}_6/\text{BiO}_{2-x}$, (d) Bi; (e) O and (f) W elements distribution.

X-ray photoelectron spectroscopy (XPS) technology was performed to elucidate the surface element composition and valence state of the prepared catalysts and the interaction between BiO_{2-x} and Bi_2WO_6 . As shown in Figure 3a, in addition to the characteristic peaks of Bi and O, there are also peaks of W in the 20% $\text{Bi}_2\text{WO}_6/\text{BiO}_{2-x}$ heterostructure. Figure 3b–d shows the XPS high-resolution spectra of O, Bi and W XPS, respectively. For $\text{Bi}_2\text{WO}_6/\text{BiO}_{2-x}$ hybrid, the deconvolution of the high-resolution spectrum of O 1s (Figure 3b) gives three peaks at 529.5 eV, 530.4 eV and 531.8 eV, assignable to lattice oxygen [42], surface hydroxyl group [37] and oxygen vacancies [43] in the as-prepared samples, respectively. The Bi 4f_{7/2} and 4f_{5/2} peaks are situated at 158.3 eV and 163.6 eV, 159.1 eV and 164.5 eV for BiO_{2-x} and Bi_2WO_6 , respectively [39]. Furthermore, the peak positions of Bi 4f for 20% $\text{Bi}_2\text{WO}_6/\text{BiO}_{2-x}$ were positively shifted relative to BiO_{2-x} , which were negatively shifted relative to Bi_2WO_6 (Figure 3c). The W 4f_{7/2} and W 4f_{5/2} peaks of 20% $\text{Bi}_2\text{WO}_6/\text{BiO}_{2-x}$ are centered at 35 eV and 37.2 eV [44], which are 0.4 eV lower than those of the Bi_2WO_6 sample (35.4 eV of W 4f_{7/2} and 37.6 eV of W 4f_{5/2}) (Figure 3d). This phenomenon reveals the successful synthesis of $\text{Bi}_2\text{WO}_6/\text{BiO}_{2-x}$ heterojunction.

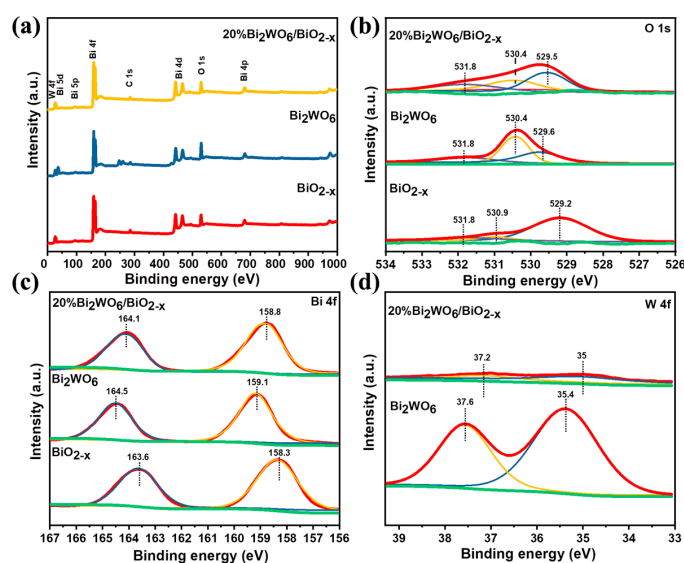


Figure 3. XPS spectrum of BiO_{2-x} , Bi_2WO_6 and 20% $\text{Bi}_2\text{WO}_6/\text{BiO}_{2-x}$: (a) survey, (b) Bi 4f, (c) O 1s and (d) W 4f.

2.2. Optical and Photoelectrochemical Property Analysis

Figure 4a displays the UV–Vis DRS spectra of the prepared photocatalysts. The absorption edge of 20% $\text{Bi}_2\text{WO}_6/\text{BiO}_{2-x}$ displayed an obvious red shift compared with that of Bi_2WO_6 , suggesting that composites could make better use of visible light. The light absorption edge of Bi_2WO_6 had a band gap of 2.54 eV, while BiO_{2-x} had a narrower band gap of 1.34 eV (Figure 4b). The positive slope of the Mott–Schottky curves in Figure S4a,b indicates that both Bi_2WO_6 and BiO_{2-x} are n-type semiconductors and the flat band positions of Bi_2WO_6 and BiO_{2-x} are -0.289 and -0.436 V (relative to Ag/AgCl). Furthermore, according to the formulas of $E_{\text{NHE}} = E_{(\text{Ag}/\text{AgCl})} + 0.197$ and $E_{\text{CB}} = E_{\text{flat band}} - 0.1$ (n-type semiconductor), the E_{CB} values of Bi_2WO_6 and BiO_{2-x} are calculated to -0.192 and -0.339 V vs. NHE, respectively. Additionally, based on the formula $E_{\text{VB}} = E_{\text{CB}} + E_g$, the valence band positions (E_{VB}) of Bi_2WO_6 and BiO_{2-x} are calculated to -2.348 and -1.001 eV vs. NHE, respectively. As shown in Figure 4c, such band combinations of Bi_2WO_6 and BiO_{2-x} were conducive to the formation of the heterojunction. Furthermore, the photoelectrochemical measurement was also evaluated to investigate the charge separation and transfer efficiency of samples. From Figure 4d, with light switching on and off, the photocurrent densities of the 20% $\text{Bi}_2\text{WO}_6/\text{BiO}_{2-x}$ composite demonstrated the highest photocurrent density over other samples, and also presented the lowest resistance ability, indicating enhanced separation of photogenerated carriers in the composites. According to the electrochemical impedance spectroscopy (EIS) Nyquist plots (Figure 4e), compared with pure Bi_2WO_6 and BiO_{2-x} , the formation of $\text{Bi}_2\text{WO}_6/\text{BiO}_{2-x}$ heterojunction could significantly reduce the semi-arc, indicating that the carrier recombination rate of the composite was lowest. In order to further detect the photogenerated electrons and holes recombination, PL emission spectra is commonly employed. As depicted in Figure 4f, the PL intensity of Bi_2WO_6 significantly decreased when it hybridized with BiO_{2-x} , indicating that the 20% $\text{Bi}_2\text{WO}_6/\text{BiO}_{2-x}$ samples obtained the superior charge separation ability. In a word, the separation efficiency of photogenerated carriers in the 20% $\text{Bi}_2\text{WO}_6/\text{BiO}_{2-x}$ samples could be greatly enhanced, which could significantly contribute to improving its photocatalytic activity.

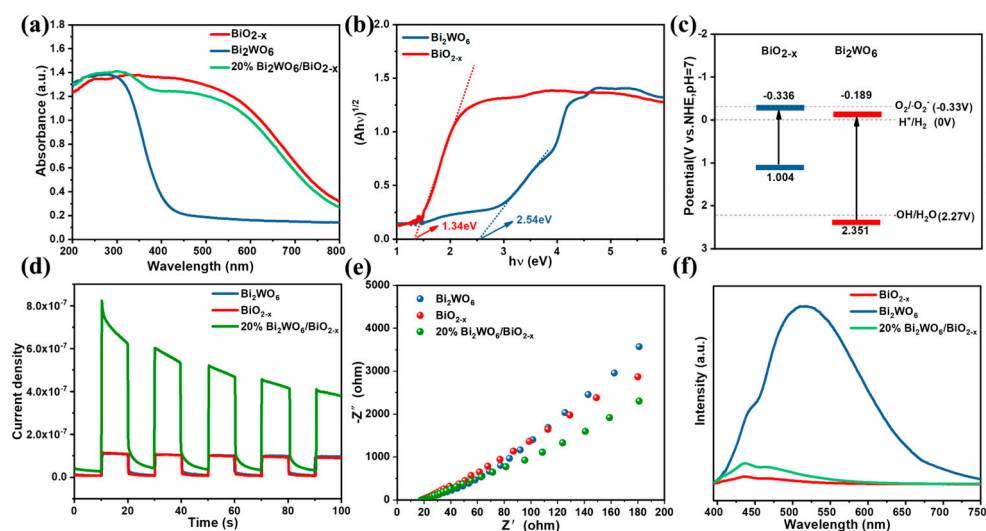


Figure 4. (a) DRS spectra of BiO_{2-x} , Bi_2WO_6 and 20% $\text{Bi}_2\text{WO}_6/\text{BiO}_{2-x}$; (b) Tauc plots, (c) Band structures of BiO_{2-x} and Bi_2WO_6 ; (d) Transient photocurrent response, (e) electrochemical impedance spectra and (f) photoluminescence fluorescence spectra of BiO_{2-x} , Bi_2WO_6 and 20% $\text{Bi}_2\text{WO}_6/\text{BiO}_{2-x}$.

2.3. Photocatalytic Performance of Catalysts

The photocatalytic performances of BiO_{2-x} , Bi_2WO_6 and a series of $\text{Bi}_2\text{WO}_6/\text{BiO}_{2-x}$ composites were explored through CIP degradation under visible light illumination. As indicated in Figure S5, no remarkable CIP decomposition was found without any catalyst

under the illumination of visible light, which indicates that the presence of catalysts is necessary for the degradation of CIP. As Figure 5a,b showed, the degradation percentage of 91.8% was achieved by 20% $\text{Bi}_2\text{WO}_6/\text{BiO}_{2-x}$ after 120 min of degradation process and its corresponding apparent kinetic constant was 0.02240 min^{-1} , which was higher than that of BiO_{2-x} by 2.37 times. Thus, the synergistic effect can be achieved using the combination of Bi_2WO_6 and BiO_{2-x} via ultrasonication, which may be ascribed to the fact that the formation of $\text{Bi}_2\text{WO}_6/\text{BiO}_{2-x}$ heterojunctions can enhance visible light absorption efficiency, accelerate the transfer rate of photo-generated electron–hole pairs and reinforce the oxidation ability for CIP decomposition.

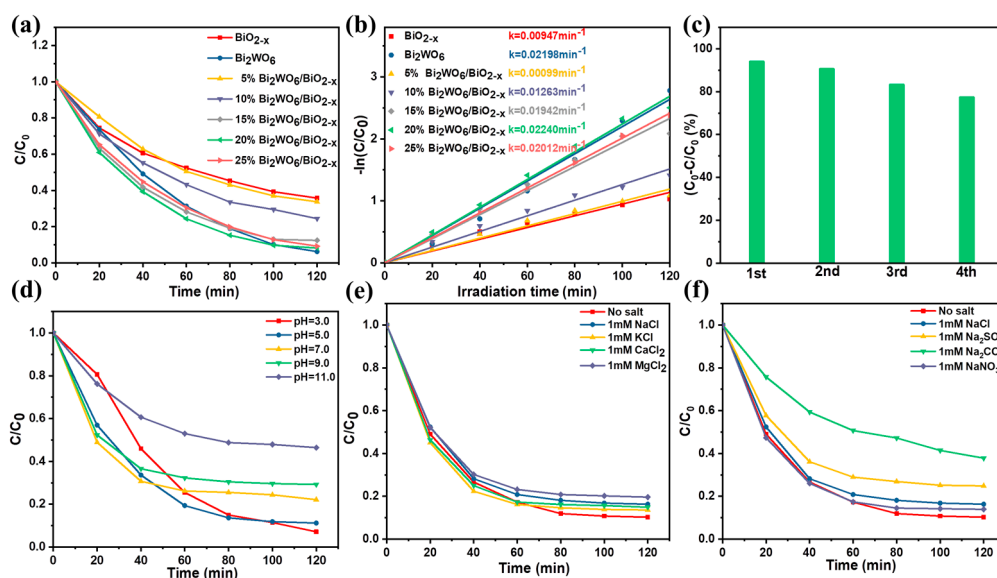


Figure 5. (a) Photocatalytic degradation of CIP using various photocatalysts irradiated with visible light and (b) their corresponding kinetic curves, (c) The cyclic experiment of the 20% $\text{Bi}_2\text{WO}_6/\text{BiO}_{2-x}$ system for degradation of CIP. The effects of (d) initial solution pH, (e) inorganic cations and (f) anions in 20% $\text{Bi}_2\text{WO}_6/\text{BiO}_{2-x}$ system for degradation of CIP under visible light irradiation. (Condition: sample dosage = 0.5 g/L, CIP concentration: 10 mg/L).

To evaluate the stability of 20% $\text{Bi}_2\text{WO}_6/\text{BiO}_{2-x}$, cyclic experiments for the photodegradation of CIP were performed in Figure 5c. 20% $\text{Bi}_2\text{WO}_6/\text{BiO}_{2-x}$ could retain its activity well for four catalytic cycles, indicating the great stability of 20% $\text{Bi}_2\text{WO}_6/\text{BiO}_{2-x}$. Moreover, the SEM image of the used 20% $\text{Bi}_2\text{WO}_6/\text{BiO}_{2-x}$ was almost the same as the fresh one (Figure S1c,d). Furthermore, in the XRD pattern before and after the photocatalytic degradation of CIP of 20% $\text{Bi}_2\text{WO}_6/\text{BiO}_{2-x}$, it was found that the position of the characteristic peak did not shift, further demonstrating the structural stability during the photocatalysis process (Figure S7). The FTIR of CIP (Figure S6a) showed peaks corresponding to the asymmetric $-\text{CH}_3$ stretching vibrations at 2924.06 cm^{-1} , ring vibrations at 1036.7 cm^{-1} , amidogen $\nu_{\text{N-H}}$ vibrations at 3600 to 2700 cm^{-1} and the $-\text{C-N}$ band finger prints of the azo nature of dye at 1119.1 cm^{-1} [45]. Most importantly, these characteristic peaks of CIP almost disappeared in the presence of 20% $\text{Bi}_2\text{WO}_6/\text{BiO}_{2-x}$ (Figure S6b–d), suggesting the degradation of CIP. These results indicated that the as-prepared 20% $\text{Bi}_2\text{WO}_6/\text{BiO}_{2-x}$ maintained stable photocatalytic activity during long time photo-degradation reactions.

As shown in Figure 5d, the influence of pH on the photo-degradation of CIP in suspensions of 20% $\text{Bi}_2\text{WO}_6/\text{BiO}_{2-x}$ was investigated in the pH range of 3.0–11.0. The dosage of 20% $\text{Bi}_2\text{WO}_6/\text{BiO}_{2-x}$ and CIP concentration were 0.5 g/L and 10 mg/L, respectively. It can be seen that when the alkalinity of the solution was increased, the degradation efficiency of CIP was inhibited. Although the CIP removal decreased at pH 11.0, about 53.6% of CIP was still removed, proving that 20% $\text{Bi}_2\text{WO}_6/\text{BiO}_{2-x}$ system could be applied over a wide pH range. According to Figure 5e, Na^+ , K^+ , Ca^{2+} and Mg^{2+} had little effect on CIP removal.

In addition, the inorganic anion NO_3^- had little effect on the degradation of CIP, while the CO_3^{2-} had a significant inhibitory effect on CIP degradation (Figure 5f). Conclusively, the 20% $\text{Bi}_2\text{WO}_6/\text{BiO}_{2-x}$ system exhibited excellent photo-degradation of organic pollutants.

2.4. Possible Degradation Pathways

In order to explore the photocatalytic degradation mechanism and possible degradation pathways of CIP, the intermediate products in the degradation of CIP were estimated using HPLC-MS. There were two possible photocatalytic degradation pathways of CIP, as shown in Figure 6. Pathway 1, CIP ($m/z = 332$), was attacked by the active species and produced the intermediates of products A ($m/z = 362$). Then, A ($m/z = 362$) suffered decarboxylation to form B ($m/z = 334$) and was further defluorinated to form E ($m/z = 344$) [46]. Subsequently, B ($m/z = 334$) lost both $-\text{CO}$ and $-\text{C}_2\text{H}_5\text{N}$ to form C ($m/z = 263$), which defluorinated to D ($m/z = 245$), respectively. F ($m/z = 316$) lost $-\text{CO}$ and was transformed to G ($m/z = 288$), which subsequently lost $-\text{C}_2\text{H}_5\text{N}$ to form D ($m/z = 245$) and formed H ($m/z = 190$) and I ($m/z = 104$) through further oxidation. Then, I ($m/z = 104$) degraded into small molecular pollutants. Pathway 2, CIP ($m/z = 332$), suffered decarboxylation to form J ($m/z = 288$). Afterward, the piperazine and adjacent $\text{C}=\text{C}$ in quinolone structure of intermediate J ($m/z = 288$) could be further oxidized and allowed the formation of intermediate K ($m/z = 243$). Then, the closing of a five-membered ring on intermediate K ($m/z = 243$) induced to the formation of intermediate L ($m/z = 181$) [47]. The side groups of the middle L ($m/z = 181$) lost with the cracking of the five-membered ring to form the middle M ($m/z = 171$). Finally, these products further oxidized and mineralized into CO_2 and H_2O .

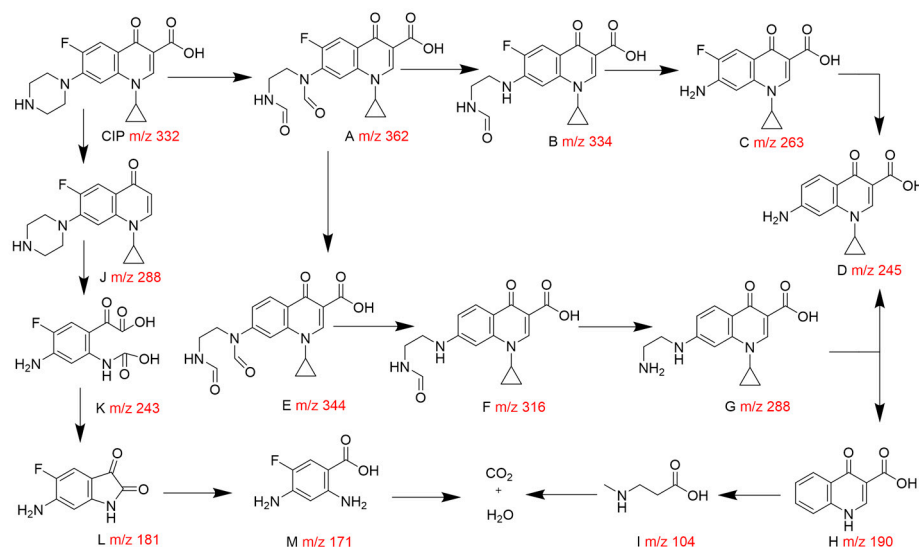


Figure 6. Proposed degradation pathways of CIP by the $\text{Bi}_2\text{WO}_6/\text{BiO}_{2-x}$ nanocomposite.

2.5. Mechanism Discussion

In order to clarify the main reactive radical species on the degradation of CIP, we carried out scavenging experiments using tertiary butanol (TBA), $\text{Na}_2\text{C}_2\text{O}_4$, p-benzoquinone (PBQ) and furfural alcohol (FFA) for quenching hydroxyl radicals ($\bullet\text{OH}$), photo-generated holes (h^+), superoxide radicals ($\bullet\text{O}_2^-$) and singlet oxygen ($^1\text{O}_2$), respectively [48]. As Figure 7a,b shows, the decomposition efficiency of CIP almost remained when TBA was added to the suspension, implying that less $\bullet\text{OH}$ was produced during CIP degradation. In contrast, a sharp decrease in decomposition efficiency was observed when $\text{Na}_2\text{C}_2\text{O}_4$, PBQ and FFA were added in system; the degradation efficiency of CIP decreased to 39.4%, 45.7% and 42.5%, and the corresponding reaction rate constant decreased to 0.00557 min^{-1} and 0.00580 min^{-1} and 0.00590 min^{-1} . These results indicated that h^+ played a major role in CIP degradation, $\bullet\text{O}_2^-$ and $^1\text{O}_2$ were the moderate reactive species in the degradation of

CIP over the 20% Bi₂WO₆/BiO_{2-x} composite. To verify this conclusion, we conducted ESR experiments in Figure 7c–f. Upon visible light illumination, the corresponding characteristic peaks intensity of DMPO-•O₂⁻, TEMP-¹O₂ and DMPO-•OH in the ESR spectra slightly increased, while the characteristic peaks' intensity of TEMPO-h⁺ decreased significantly after illumination. As illustrated in Figure 7e, the three peaks' intensity of TEMPO-h⁺ would get weaker, demonstrating the existence of photogenerated h⁺ [6]. Conclusively, the existence of •O₂⁻, ¹O₂, •OH and h⁺ in CIP photodegradation process was confirmed.

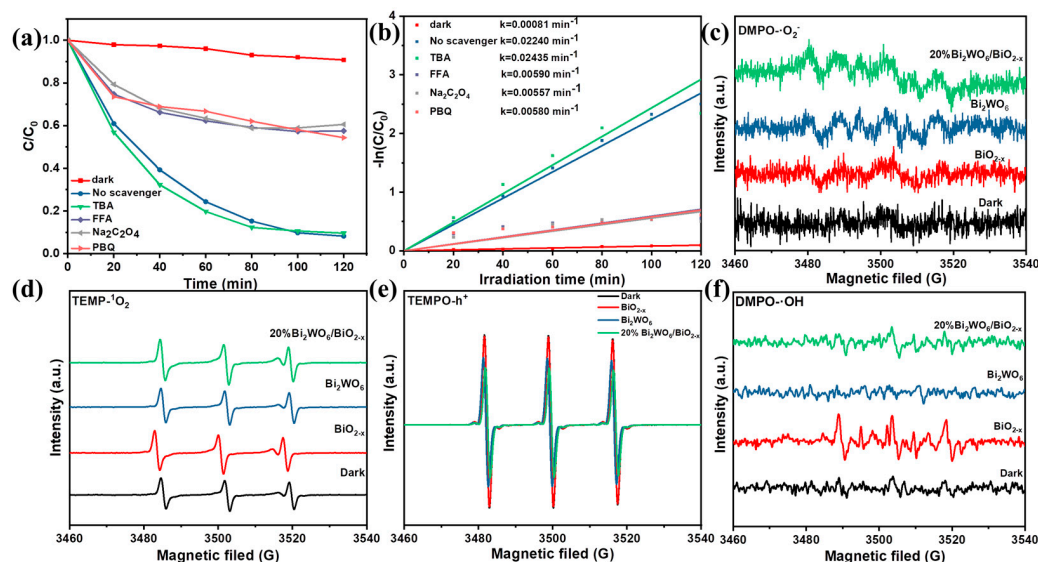
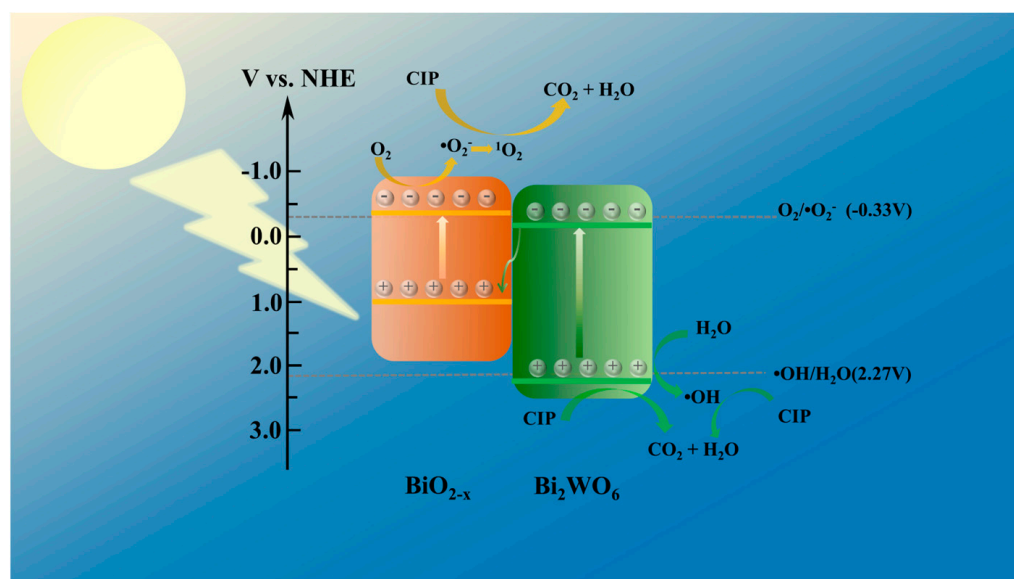


Figure 7. (a) Photodegradation of CIP in a 20% Bi₂WO₆/BiO_{2-x} system with different quenchers and (b) corresponding kinetic plots. ESR spectra of various catalysts for (c) DMPO-•O₂⁻ adduct; (d) TEMP-¹O₂ adduct; (e) TEMPO-h⁺ adduct and (f) DMPO-•OH adduct.

According to the aforementioned results, the possible CIP photodegradation mechanism was presented in Scheme 1. Under visible light irradiation, both Bi₂WO₆ and BiO_{2-x} could be photoexcited and produced electron–hole pairs, and the photo-induced electrons migrated from the valence band to the conduction band. Since the E_{CB} of Bi₂WO₆ was more positive than the O₂/•O₂⁻ potential (−0.33 V vs. NHE), •O₂⁻ could not be generated in the CB. Therefore, the type II heterojunction did not conform to the structure of this Bi₂WO₆/BiO_{2-x} composites, that a Z-scheme charge transfer way was proposed for this degradation process. The photogenerated electrons in the CB of Bi₂WO₆ could migrate to the VB of BiO_{2-x} and combine with h⁺ by visible light illuminating. In the VB of Bi₂WO₆ and the CB of BiO_{2-x}, •OH and •O₂⁻ could be produced, respectively. Moreover, most of the •O₂⁻ further reacted to generate ¹O₂. These active species gradually converted CIP into small molecules that were easily broken down. Combined with ESR and radical quenching reactions, the overall electron transition and CIP degradation reaction in Bi₂WO₆/BiO_{2-x} heterostructures were proposed as follows (Equations (1)–(7)) [49–51]:





Scheme 1. The proposed photocatalytic mechanism for photodegradation of CIP over the $\text{Bi}_2\text{WO}_6/\text{BiO}_{2-x}$ composites.

3. Experimental

3.1. Materials

$\text{NaBiO}_3 \cdot 2\text{H}_2\text{O}$, $\text{Bi}(\text{NO}_3)_3 \cdot 5\text{H}_2\text{O}$, $\text{Na}_2\text{WO}_4 \cdot 2\text{H}_2\text{O}$, tertiary butanol, $\text{Na}_2\text{C}_2\text{O}_4$ and p-benzoquinone were purchased from Sinopharm Chemical Reagent Co., Ltd. (Shanghai, China). Ethylene glycol and furfural alcohol were purchased from Aladdin Reagents Co., Ltd. (Shanghai, China). Ciprofloxacin hydrochloride monohydrate was used as CIP raw material, which was produced by the Sinopharm Chemical Reagent Co., Ltd. (Shanghai, China).

3.2. Preparation of BiO_{2-x}

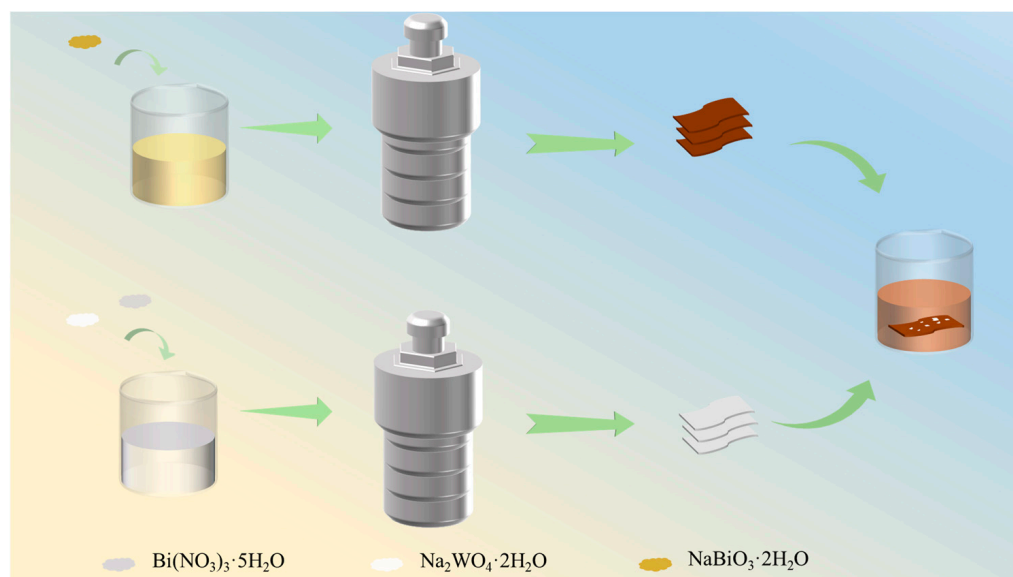
BiO_{2-x} was prepared using a hydrothermal method. Briefly, 1.2 g NaOH and 1.4 g $\text{NaBiO}_3 \cdot 2\text{H}_2\text{O}$ were incorporated into 30 mL of ultrapure water via magnetic stirring. After stirring for 30 min, the suspension was transferred into a 50 mL autoclave, and heated at 180 °C for 18 h. The mixture was naturally cooled to room temperature and collected via centrifugation, washed with ultrapure water and dried at 80 °C for 4 h under vacuum.

3.3. Preparation of Bi_2WO_6

Firstly, 0.3881 g $\text{Bi}(\text{NO}_3)_3 \cdot 5\text{H}_2\text{O}$ and 0.1319 g $\text{Na}_2\text{WO}_4 \cdot 2\text{H}_2\text{O}$ were mixed together in 40 mL of ethylene glycol and stirred for 30 min to obtain the homogeneous solution. It was transferred into a 100 mL Teflon-lined autoclave and treated at 160 °C for 15 h. After cooling at 25 °C, the product was centrifuged and rinsed several times with ethanol and ultrapure water to remove residual inorganic ions. Finally, Bi_2WO_6 powders were oven-dried at 70 °C for 12 h.

3.4. Preparation of $\text{Bi}_2\text{WO}_6/\text{BiO}_{2-x}$

The $\text{Bi}_2\text{WO}_6/\text{BiO}_{2-x}$ composite was prepared via an electrostatic self-assembly method illustrated in Scheme 2. A total of 0.10 g of BiO_{2-x} and different amounts of Bi_2WO_6 (0.005, 0.01, 0.015, 0.02 and 0.025 g) were added to 30 mL ethanol with ultrasonics for 4 h, and dried at 60 °C for 4 h under vacuum.



Scheme 2. Schematic illustration of the preparation of $\text{Bi}_2\text{WO}_6/\text{BiO}_{2-x}$ composites.

4. Conclusions

In summary, we have successfully prepared a Z-scheme $\text{Bi}_2\text{WO}_6/\text{BiO}_{2-x}$ heterostructures using a simple method with excellent photocatalytic CIP degradation performance under visible light irradiation. By constructing a Z-scheme heterostructure, the charge recombination rate was significantly reduced in the photocatalytic degradation of ciprofloxacin. The Z-scheme charge transfer mechanism in $\text{Bi}_2\text{WO}_6/\text{BiO}_{2-x}$ heterojunction as investigated via XPS, photoelectrochemical measurements and ESR experiment greatly enhances the separation of photogenerated carriers to expedite CIP photodegradation. With the increasing Bi_2WO_6 content, the average grain size of the samples decreases, and the surface area of the materials in contact with the pollutant increases, which improves the photocatalytic performance. The 20% $\text{Bi}_2\text{WO}_6/\text{BiO}_{2-x}$ samples were constructed to alleviate the problem of the high recombination rate of photogenerated $e^- \cdot h^+$, and the CIP degradation rate reaches 91.8% under the present conditions. The 20% $\text{Bi}_2\text{WO}_6/\text{BiO}_{2-x}$ heterostructures still had good stability and photocatalytic activity after four cycles, showing high potential in practical applications. Critically, this study demonstrates the successful application of CIP degradation and provides valuable insights regarding the development of the construction of heterojunctions to further improve their photocatalytic degradation efficiency.

Supplementary Materials: The following supporting information can be downloaded at: <https://www.mdpi.com/article/10.3390/catal13030469/s1>, Table S1: Crystallite size of the prepared materials [17]; Table S2: Porous parameters of BiO_{2-x} , Bi_2WO_6 and 20% $\text{Bi}_2\text{WO}_6/\text{BiO}_{2-x}$ [15]; Figure S1: SEM image of (a) BiO_{2-x} ; (b) Bi_2WO_6 ; 20% $\text{Bi}_2\text{WO}_6/\text{BiO}_{2-x}$ (c) before and (d) after use [5]; Figure S2: TEM images of (a) BiO_{2-x} ; (c) Bi_2WO_6 and HRTEM images of (b) BiO_{2-x} ; (d) Bi_2WO_6 [47]; Figure S3: EDX spectrum of 20% $\text{Bi}_2\text{WO}_6/\text{BiO}_{2-x}$ [48]; Figure S4: The Mott-Schottky plots of (a) Bi_2WO_6 and (b) BiO_{2-x} at different frequencies (500 Hz, 1000 Hz and 1500 Hz) [41]; Figure S5: Photocatalytic degradation of CIP without any catalyst for comparison tests. (condition: sample dosage = 0.5 g/L, CIP concentration: 10 mg/L) [1]; Figure S6: FT-IR spectra of (a) CIP, (b) 20% $\text{Bi}_2\text{WO}_6/\text{BiO}_{2-x}$ (c) 20% $\text{Bi}_2\text{WO}_6/\text{BiO}_{2-x}$ after mixing with CIP in the dark for 30 min, and (d) 20% $\text{Bi}_2\text{WO}_6/\text{BiO}_{2-x}$ after mixing with CIP in the dark for 30 min and then under visible light irradiation for 2 h [52]; Figure S7: XRD patterns of BiO_{2-x} , Bi_2WO_6 , fresh and used $\text{Bi}_2\text{WO}_6/\text{BiO}_{2-x}$ composites [53]; Figure S8: Bode plots of BiO_{2-x} , Bi_2WO_6 and 20% $\text{Bi}_2\text{WO}_6/\text{BiO}_{2-x}$ [54]; Figure S9: Photocatalytic degradation of CIP with prolonged light time for comparison test. (condition: sample dosage = 0.5 g/L, CIP concentration: 10 mg/L) [55]; Table S3. The catalytic performance comparison of recently reported catalysts for CIP degradation based on reduction percentages and reaction time.

Author Contributions: Conceptualization, H.Z. and J.L.; methodology, software, validation, formal analysis, investigation, resources, H.Z.; data curation, writing—original draft preparation, H.Z. and Z.F.; writing—review and editing, visualization, Z.F. and Q.C. All authors have read and agreed to the published version of the manuscript.

Funding: This research was funded by the Outstanding Talent Research Fund of Zhengzhou University, China Postdoctoral Science Foundation (No. 2020TQ0277, 2020M682328), China Scholarship Council (No. 202108410356), and Postdoctoral Science Foundation of Henan province (No. 202002010).

Data Availability Statement: Data Availability Statements are available in section “MDPI Research Data Policies” at <https://www.mdpi.com/ethics> (accessed on 1 February 2023).

Conflicts of Interest: The authors declare no conflict of interest.

References

1. Wang, J.; Chang, X.; Zhao, Y.; Xu, H.; He, G.; Chen, H. A novel Bi₂WO₆/BiOBr/RGO photocatalyst for enhanced degradation of ciprofloxacin under visible light irradiation: Performance, mechanism and toxicity evaluation. *Diam. Relat. Mater.* **2022**, *128*, 109274. [CrossRef]
2. Zhu, J.; Wang, H.; Duan, A.; Wang, Y. Mechanistic insight into the degradation of ciprofloxacin in water by hydroxyl radicals. *J. Hazard. Mater.* **2022**, *446*, 130676. [CrossRef] [PubMed]
3. Zhu, Z.; Xia, H.; Li, X.; Li, H. A novel 1D/2D rod-sheet shape Cu₃Mo₂O₉/g-C₃N₄ heterojunction photocatalyst with enhanced photocatalytic performance for ciprofloxacin. *Opt. Mater.* **2023**, *136*, 113420. [CrossRef]
4. Feng, N.X.; Yu, J.; Xiang, L.; Yu, L.Y.; Zhao, H.M.; Mo, C.H.; Li, Y.W.; Cai, Q.Y.; Wong, M.H.; Li, Q.X. Co-metabolic degradation of the antibiotic ciprofloxacin by the enriched bacterial consortium XG and its bacterial community composition. *Sci. Total Environ.* **2019**, *665*, 41–51. [CrossRef]
5. Hu, H.; Xu, C.; Jin, J.; Xu, M.; Cheng, Y.; Ji, W.; Ding, Z.; Shao, M.; Wan, Y. Synthesis of a BiOIO₃/Bi₂O₄ heterojunction that can efficiently degrade rhodamine B and ciprofloxacin under visible light. *Opt. Mater.* **2022**, *133*, 112893. [CrossRef]
6. Zhang, X.; Liu, J.; Zheng, X.; Chen, R.; Zhang, M.; Liu, Z.; Wang, Z.; Li, J. Activation of oxalic acid via dual-pathway over single-atom Fe catalysts: Mechanism and membrane application. *Appl. Catal. B Environ.* **2023**, *321*, 122068. [CrossRef]
7. Arif, M.; Zhang, M.; Mao, Y.; Bu, Q.; Ali, A.; Qin, Z.; Muhmood, T.; Shahnoor; Liu, X.; Zhou, B.; et al. Oxygen vacancy mediated single unit cell Bi₂WO₆ by Ti doping for ameliorated photocatalytic performance. *J. Colloid Interface Sci.* **2021**, *581*, 276–291. [CrossRef]
8. Bai, Y.; Mao, W.; Wu, Y.; Gao, Y.; Wang, T.; Liu, S. Synthesis of novel ternary heterojunctions via Bi₂WO₆ coupling with CuS and g-C₃N₄ for the highly efficient visible-light photodegradation of ciprofloxacin in wastewater. *Colloids Surf. A* **2021**, *610*, 125481. [CrossRef]
9. Tian, Y.; Zhang, J.; Wang, W.; Liu, J.; Zheng, X.; Li, J.; Guan, X. Facile assembly and excellent elimination behavior of porous BiOBr-g-C₃N₄ heterojunctions for organic pollutants. *Environ. Res.* **2022**, *209*, 112889. [CrossRef]
10. Wu, S.; Sun, J.; Li, Q.; Hood, Z.D.; Yang, S.; Su, T.; Peng, R.; Wu, Z.; Sun, W.; Kent, P.R.C.; et al. Effects of Surface Terminations of 2D Bi₂WO₆ on Photocatalytic Hydrogen Evolution from Water Splitting. *ACS Appl. Mater. Interfaces* **2020**, *12*, 20067–20074. [CrossRef]
11. Lv, Y.R.; Wang, Z.L.; Yang, Y.X.; Luo, Y.; Yang, S.Y.; Xu, Y.H. Tin bisulfide nanoplates anchored onto flower-like bismuth tungstate nanosheets for enhancement in the photocatalytic degradation of organic pollutant. *J. Hazard. Mater.* **2022**, *432*, 128665. [CrossRef]
12. Su, H.; Li, S.; Xu, L.; Liu, C.; Zhang, R.; Tan, W. Hydrothermal preparation of flower-like Ni²⁺ doped Bi₂WO₆ for enhanced photocatalytic degradation. *J. Phys. Chem. Solids* **2022**, *170*, 110954. [CrossRef]
13. Bai, J.; Zhang, B.; Xiong, T.; Jiang, D.; Ren, X.; Lu, P.; Fu, M. Enhanced visible light driven photocatalytic performance of Bi₂WO₆ nano-catalysts by introducing oxygen vacancy. *J. Alloys Compd.* **2021**, *887*, 161297. [CrossRef]
14. Wu, X.; Zhang, W.; Li, J.; Xiang, Q.; Liu, Z.; Liu, B. Identification of the Active Sites on Metallic MoO_{2-x} Nano-Sea-Urchin for Atmospheric CO₂ Photoreduction Under UV, Visible, and Near-Infrared Light Illumination. *Angew. Chem. Int. Ed. Engl.* **2022**, *62*, e202213124. [PubMed]
15. Zhang, M.; Lai, C.; Li, B.; Huang, D.; Liu, S.; Qin, L.; Yi, H.; Fu, Y.; Xu, F.; Li, M.; et al. Ultrathin oxygen-vacancy abundant WO₃ decorated monolayer Bi₂WO₆ nanosheet: A 2D/2D heterojunction for the degradation of Ciprofloxacin under visible and NIR light irradiation. *J. Colloid Interface Sci.* **2019**, *556*, 557–567. [CrossRef]
16. Li, J.; Huang, B.; Guo, Q.; Guo, S.; Peng, Z.; Liu, J.; Tian, Q.; Yang, Y.; Xu, Q.; Liu, Z.; et al. Van der Waals heterojunction for selective visible-light-driven photocatalytic CO₂ reduction. *Appl. Catal. B Environ.* **2021**, *284*, 119733. [CrossRef]
17. Kumar, G.; Dutta, R.K. Fabrication of plate-on-plate SnS₂/Bi₂WO₆ nanocomposite as photocatalyst for sunlight mediated degradation of antibiotics in aqueous medium. *J. Phys. Chem. Solids* **2022**, *164*, 110639. [CrossRef]
18. Su, Y.; Tan, G.; Liu, T.; Lv, L.; Wang, Y.; Zhang, X.; Yue, Z.; Ren, H.; Xia, A. Photocatalytic properties of Bi₂WO₆/BiPO₄ Z-scheme photocatalysts induced by double internal electric fields. *Appl. Surf. Sci.* **2018**, *457*, 104–114. [CrossRef]

19. Arif, M.; Min, Z.; Yuting, L.; Yin, H.; Liu, X. A Bi_2WO_6 -based hybrid heterostructures photocatalyst with enhanced photodecomposition and photocatalytic hydrogen evolution through Z-scheme process. *J. Ind. Eng. Chem.* **2019**, *69*, 345–357. [[CrossRef](#)]
20. Li, Z.; Chen, M.; Zhang, Q.; Tao, D. Mechanochemical synthesis of a Z-scheme $\text{Bi}_2\text{WO}_6/\text{CuBi}_2\text{O}_4$ heterojunction and its visible-light photocatalytic degradation of ciprofloxacin. *J. Alloys Compd.* **2020**, *845*, 156291. [[CrossRef](#)]
21. Li, S.; Chen, J.; Hu, S.; Wang, H.; Jiang, W.; Chen, X. Facile construction of novel $\text{Bi}_2\text{WO}_6/\text{Ta}_3\text{N}_5$ Z-scheme heterojunction nanofibers for efficient degradation of harmful pharmaceutical pollutants. *Chem. Eng. J.* **2020**, *402*, 126165. [[CrossRef](#)]
22. Huang, Y.; Kou, S.; Zhang, X.; Wang, L.; Lu, P.; Zhang, D. Facile Fabrication of Z-Scheme $\text{Bi}_2\text{WO}_6/\text{WO}_3$ Composites for Efficient Photodegradation of Bisphenol A with Peroxymonosulfate Activation. *Nanomaterials* **2020**, *10*, 724. [[CrossRef](#)] [[PubMed](#)]
23. Mahammed Shaheer, A.R.; Thangavel, N.; Rajan, R.; Abraham, D.A.; Vinoth, R.; Sunaja Devi, K.R.; Shankar, M.V.; Neppolian, B. Sonochemical assisted impregnation of Bi_2WO_6 on TiO_2 nanorod to form Z-scheme heterojunction for enhanced photocatalytic H_2 production. *Adv. Powder Technol.* **2021**, *32*, 4734–4743. [[CrossRef](#)]
24. Chin, Y.-H.; Sin, J.-C.; Lam, S.-M.; Zeng, H.; Lin, H.; Li, H.; Huang, L.; Mohamed, A.R. 3-D/3-D Z-Scheme Heterojunction Composite Formed by Marimo-like Bi_2WO_6 and Mammillaria-like ZnO for Expeditious Sunlight Photodegradation of Dimethyl Phthalate. *Catalysts* **2022**, *12*, 1427. [[CrossRef](#)]
25. Wang, K.; Wang, Q.; Zhang, K.; Wang, G.; Wang, H. Selective solar-driven CO_2 reduction mediated by 2D/2D $\text{Bi}_2\text{O}_2\text{SiO}_3/\text{MXene}$ nanosheets heterojunction. *J. Mater. Sci. Technol.* **2022**, *124*, 202–208. [[CrossRef](#)]
26. Wang, K.; Du, Y.; Li, Y.; Wu, X.; Hu, H.; Wang, G.; Xiao, Y.; Chou, S.; Zhang, G. Atomic-level insight of sulfidation-engineered Aurivillius-related $\text{Bi}_2\text{O}_2\text{SiO}_3$ nanosheets enabling visible light low-concentration CO_2 conversion. *Carbon Energy* **2022**, *5*, e264. [[CrossRef](#)]
27. Wang, K.; Shao, X.; Zhang, K.; Wang, J.; Wu, X.; Wang, H. 0D/3D $\text{Bi}_3\text{TaO}_7/\text{ZnIn}_2\text{S}_4$ heterojunction photocatalyst towards degradation of antibiotics coupled with simultaneous H_2 evolution: In situ irradiated XPS investigation and S-scheme mechanism insight. *Appl. Surf. Sci.* **2022**, *596*, 153444. [[CrossRef](#)]
28. He, N.; Guo, Z.; Zhang, C.; Yu, Y.; Tan, L.; Luo, H.; Li, L.; Bahnmann, J.; Chen, H.; Jiang, F. Bifunctional 2D/2D g- $\text{C}_3\text{N}_4/\text{BiO}_{2-x}$ nanosheets heterojunction for bacterial disinfection mechanisms under visible and near-infrared light irradiation. *J. Hazard. Mater.* **2022**, *436*, 129123. [[CrossRef](#)]
29. Son, H.; Kim, Y. Near-infrared driven photocatalyst ($\text{Ag}/\text{BiO}_{2-x}$) with post-illumination catalytic memory. *J. Phys. Chem. Solids* **2022**, *167*, 110781. [[CrossRef](#)]
30. Liu, J.; Zhang, X.; Zhong, Q.; Li, J.; Wu, H.; Zhang, B.; Jin, L.; Tao, H.B.; Liu, B. Electrostatic self-assembly of a $\text{AgI}/\text{Bi}_2\text{Ga}_4\text{O}_9$ p-n junction photocatalyst for boosting superoxide radical generation. *J. Mater. Chem. A* **2020**, *8*, 4083–4090. [[CrossRef](#)]
31. Tian, Y.; Li, J.; Zheng, H.; Guan, X.; Zhang, X.; Zheng, X. Synthesis and enhanced photocatalytic performance of Ni^{2+} -doped Bi_4O_7 nanorods with broad-spectrum photoresponse. *Sep. Purif. Technol.* **2022**, *300*, 121898. [[CrossRef](#)]
32. Li, J.; Li, Y.; Zhang, G.; Huang, H.; Wu, X. One-Dimensional/Two-Dimensional Core-Shell-Structured $\text{Bi}_2\text{O}_4/\text{BiO}_{2-x}$ Heterojunction for Highly Efficient Broad Spectrum Light-Driven Photocatalysis: Faster Interfacial Charge Transfer and Enhanced Molecular Oxygen Activation Mechanism. *ACS Appl. Mater. Interfaces* **2019**, *11*, 7112–7122. [[CrossRef](#)] [[PubMed](#)]
33. Jin, J.; Sun, J.; Lv, K.; Guo, X.; Hou, Q.; Liu, J.; Wang, J.; Bai, Y.; Huang, X. Oxygen vacancy $\text{BiO}_{2-x}/\text{Bi}_2\text{WO}_6$ synchronous coupling with Bi metal for phenol removal via visible and near-infrared light irradiation. *J. Colloid Interface Sci.* **2022**, *605*, 342–353. [[CrossRef](#)] [[PubMed](#)]
34. Li, G.; Lian, Z.; Wan, Z.; Liu, Z.; Qian, J.; Deng, Y.; Zhang, S.; Zhong, Q. Efficient photothermal-assisted photocatalytic NO removal on molecular cobalt phthalocyanine/ Bi_2WO_6 Z-scheme heterojunctions by promoting charge transfer and oxygen activation. *Appl. Catal. B Environ.* **2022**, *317*, 121787. [[CrossRef](#)]
35. Xiong, S.; Bao, S.; Wang, W.; Hao, J.; Mao, Y.; Liu, P.; Huang, Y.; Duan, Z.; Lv, Y.; Ouyang, D. Surface oxygen vacancy and graphene quantum dots co-modified Bi_2WO_6 toward highly efficient photocatalytic reduction of CO_2 . *Appl. Catal. B Environ.* **2022**, *305*, 121026. [[CrossRef](#)]
36. Niu, R.; Liu, Q.; Huang, B.; Liu, Z.; Zhang, W.; Peng, Z.; Wang, Z.; Yang, Y.; Gu, Z.; Li, J. Black phosphorus/ $\text{Bi}_{19}\text{Br}_3\text{S}_{27}$ van der Waals heterojunctions ensure the supply of activated hydrogen for effective CO_2 photoreduction. *Appl. Catal. B Environ.* **2022**, *317*, 121727. [[CrossRef](#)]
37. Huang, Y.; Kang, S.; Yang, Y.; Qin, H.; Ni, Z.; Yang, S.; Li, X. Facile synthesis of $\text{Bi}/\text{Bi}_2\text{WO}_6$ nanocomposite with enhanced photocatalytic activity under visible light. *Appl. Catal. B Environ.* **2016**, *196*, 89–99. [[CrossRef](#)]
38. Jakhade, A.P.; Biware, M.V.; Chikate, R.C. Two-Dimensional Bi_2WO_6 Nanosheets as a Robust Catalyst toward Photocyclization. *ACS Omega* **2017**, *2*, 7219–7229. [[CrossRef](#)]
39. Li, J.; Wang, J.; Zhang, G.; Li, Y.; Wang, K. Enhanced molecular oxygen activation of Ni^{2+} -doped BiO_{2-x} nanosheets under UV, visible and near-infrared irradiation: Mechanism and DFT study. *Appl. Catal. B Environ.* **2018**, *234*, 167–177. [[CrossRef](#)]
40. Liu, J.; Liu, Q.; Li, J.; Zheng, X.; Liu, Z.; Guan, X. Photochemical conversion of oxalic acid on heterojunction engineered $\text{FeWO}_4/\text{g-C}_3\text{N}_4$ photocatalyst for high-efficient synchronous removal of organic and heavy metal pollutants. *J. Clean. Prod.* **2022**, *363*, 132527. [[CrossRef](#)]
41. Bai, L.; Cao, Y.; Pan, X.; Shu, Y.; Dong, G.; Zhao, M.; Zhang, Z.; Wu, Y.; Wang, B. Z-scheme $\text{Bi}_2\text{S}_3/\text{Bi}_2\text{O}_2\text{CO}_3$ nanoheterojunction for the degradation of antibiotics and organic compounds in wastewater: Fabrication, application, and mechanism. *Surf. Interfaces.* **2023**, *36*, 102612. [[CrossRef](#)]

42. Li, J.; Wu, X.; Pan, W.; Zhang, G.; Chen, H. Vacancy-Rich Monolayer BiO_{2-x} as a Highly Efficient UV, Visible, and Near-Infrared Responsive Photocatalyst. *Angew. Chem. Int. Ed. Engl.* **2018**, *57*, 491–495. [[CrossRef](#)] [[PubMed](#)]
43. Huang, X.-H.; Zhang, L.; Song, J.; Cao, X.-F.; Guo, Y.-C. Novel nanoparticle-assembled Bi₁₂GeO₂₀ hierarchical structures: Facile hydrothermal synthesis and excellent photocatalytic activity. *RSC Adv.* **2016**, *6*, 92560–92568. [[CrossRef](#)]
44. Tian, J.; Sang, Y.; Yu, G.; Jiang, H.; Mu, X.; Liu, H. A Bi₂WO₆-based hybrid photocatalyst with broad spectrum photocatalytic properties under UV, visible, and near-infrared irradiation. *Adv. Mater.* **2013**, *25*, 5075–5080. [[CrossRef](#)] [[PubMed](#)]
45. Li, Y.; Fu, Y.; Zhu, M. Green synthesis of 3D tripyramid TiO₂ architectures with assistance of aloe extracts for highly efficient photocatalytic degradation of antibiotic ciprofloxacin. *Appl. Catal. B Environ.* **2020**, *260*, 118149. [[CrossRef](#)]
46. Li, Y.; Chen, L.; Tian, X.; Lin, L.; Ding, R.; Yan, W.; Zhao, F. Functional role of mixed-culture microbe in photocatalysis coupled with biodegradation: Total organic carbon removal of ciprofloxacin. *Sci. Total Environ.* **2021**, *784*, 147049. [[CrossRef](#)]
47. Yu, X.; Zhang, J.; Zhang, J.; Niu, J.; Zhao, J.; Wei, Y.; Yao, B. Photocatalytic degradation of ciprofloxacin using Zn-doped Cu₂O particles: Analysis of degradation pathways and intermediates. *Chem. Eng. J.* **2019**, *374*, 316–327. [[CrossRef](#)]
48. Xu, K.; Shen, J.; Zhang, S.; Xu, D.; Chen, X. Efficient interfacial charge transfer of BiOCl-In₂O₃ step-scheme heterojunction for boosted photocatalytic degradation of ciprofloxacin. *J. Mater. Sci. Technol.* **2022**, *121*, 236–244. [[CrossRef](#)]
49. Hu, K.; Li, R.; Ye, C.; Wang, A.; Wei, W.; Hu, D.; Qiu, R.; Yan, K. Facile synthesis of Z-scheme composite of TiO₂ nanorod/g-C₃N₄ nanosheet efficient for photocatalytic degradation of ciprofloxacin. *J. Clean. Prod.* **2020**, *253*, 120055. [[CrossRef](#)]
50. Zhu, C.; Zhang, Y.; Fan, Z.; Liu, F.; Li, A. Carbonate-enhanced catalytic activity and stability of Co₃O₄ nanowires for ¹O₂-driven bisphenol A degradation via peroxymonosulfate activation: Critical roles of electron and proton acceptors. *J. Hazard. Mater.* **2020**, *393*, 122395. [[CrossRef](#)]
51. Gao, K.; Hou, L.-A.; An, X.; Huang, D.; Yang, Y. BiOBr/MXene/g-C₃N₄ Z-scheme heterostructure photocatalysts mediated by oxygen vacancies and MXene quantum dots for tetracycline degradation: Process, mechanism and toxicity analysis. *Appl. Catal. B Environ.* **2023**, *323*, 122150. [[CrossRef](#)]
52. Karim, A.V.; Shrivastav, A. Degradation of ciprofloxacin using photo, sono, and sonophotocatalytic oxidation with visible light and low-frequency ultrasound: Degradation kinetics and pathways. *Chem. Eng. J.* **2020**, *392*, 124853. [[CrossRef](#)]
53. Mao, J.; Hong, B.; Wei, J.; Xu, J.; Han, Y.; Jin, H.; Jin, D.; Peng, X.; Li, J.; Yang, Y.; et al. Enhanced Ciprofloxacin Photodegradation of Visible-Light-Driven Z-Scheme g-C₃N₄/Bi₂WO₆ Nanocomposites and Interface Effect. *ChemistrySelect* **2019**, *4*, 13716–13723. [[CrossRef](#)]
54. Wen, R.; Yang, L.; Wu, S.; Zhou, D.; Jiang, B. Tuning surface sites to boost photocatalytic degradation of phenol and ciprofloxacin. *Chin. Chem. Lett.* **2023**, *34*, 107204. [[CrossRef](#)]
55. Chen, X.; Gao, X.; Ai, L.; Fan, H. Triton X-100-assisted synthesis of layered nanosheet-assembled flower-like BiOBr nanostructures with enhanced visible-light photocatalytic degradation of ciprofloxacin. *J. Nanopart. Res.* **2022**, *24*, 103. [[CrossRef](#)]

Disclaimer/Publisher's Note: The statements, opinions and data contained in all publications are solely those of the individual author(s) and contributor(s) and not of MDPI and/or the editor(s). MDPI and/or the editor(s) disclaim responsibility for any injury to people or property resulting from any ideas, methods, instructions or products referred to in the content.